UNIVERSITY OF HAWAIʻI

# Modeling Coral Breakage at Kure Atoll

A THESIS SUBMITTED TO
THE GLOBAL ENVIRONMENTAL SCIENCE
UNDERGRADUATE DIVISION IN PARTIAL FULFILLMENT
OF THE REQUIREMENTS FOR THE DEGREE OF

BACHELOR OF SCIENCE

IN

GLOBAL ENVIRONMENTAL SCIENCE

AUGUST 2014

BY
ERIC MASA SHIMABUKURO

THESIS ADVISOR:
JAMES T. POTEMRA, PHD.
HAWAII INSTITUTE OF GEOPHYSICS AND PLANETOLOGY

I certify that I have read this thesis and that, in my opinion, it is satisfactory in scope and quality as a thesis for the degree of Bachelor of Science in Global Environmental Science.

Dr. James T. Potemra
Hawaii Institute of Geophysics and Planetology

This thesis is dedicated to the hopes and dreams of my grandmother Shikako, my father Norman, and my mother Laura.

# Acknowledgements

I would like to thank Dr. James Potemra, for consistent patience, guidance, editing and motivation; Dr. Jane Schoonmaker, for editing suggestions and encouragement; my mother Laura, for support in the darkest of times; Will McGrath for being a voice of reason; Jennifer Killinger, for patience when I needed it most; the many members of the Pacific Islands Benthic Habitat Mapping Center and operators of the research vessels for gathering the bathymetry data on which all oceanographic models rely; and the many students of the Global Environmental Science program.

# Abstract

Given the current state of climate change, coral reefs throughout the world are under increasing pressure to survive. One factor influencing the development of coral reef ecosystems is the energy of the surface waves passing above them. The waves cause the water particles beneath them to flow in elliptical orbits, and the bottom of these orbits can create strong flows which can cause coral fingers to break off. This study follows the work of Storlazzi et al. [2005] in an attempt to model the likelihood of coral breakage at Kure Atoll. To accomplish this, the wave field is modeled using the third generation wave model Simulating Waves Nearshore (SWAN) [Booij et al. 1999], with boundary conditions and wind forcing provided by WaveWatch III [Tolman 2002]. The SWAN results for the velocity of the wave orbitals are fed into the hydrodynamic 'Force Balance Model' of Storlazzi et al. [2005], which estimates the applied stress of the water on the coral, and compares this with measured mechanical strengths. The results, which differ from Storlazzi et al. [2005], indicate that the corals of Kure Atoll are well suited to their environment, and are hardy enough to withstand typical wave conditions year round. Additionally, the extreme event results indicate that corals can withstand open ocean wave heights of up to nine meters, due in part to the fact that high resolution modeling indicates that some of the wave energy is lost as the waves approach the shallow coral reef zones. Finally, this study highlights the need for extensive documentation in the presentation of mathematical models: because the documentation of Storlazzi

et al. [2005] did not explicitly define all equations utilized, it is impossible to completely compare the results of this study and the previous one, leaving questions as to why the results differ so greatly.

# Contents

## List of Tables

# List of Figures

# 1 Introduction

Coral reefs exist in a dynamic environment and are subject to a wide range of highly variable environmental forcings [Gove et al. 2011]. In the Hawaiian islands, corals and coralline algae compose the physical baseline of the reefs, and are foundational to the entire ecosystem [Grigg 1998]. Because of this, coral vigor and abundance is often a good indicator of the health of the entire reef [Jokiel and Rodgers 2007]. Therefore, it is important to assess the factors influencing coral health, both to establish baselines for comparative studies and to understand proper management practices [Kenyon et al. 2008].

When considering the factors that influence corals, one cannot fully describe the environment without an inclusion of the constant movement of the medium in which corals grow—i.e. the wave motions of the reef zone. To that end, there have been a collection of studies that examined the qualitative relationship between wave energy and coral distributions [Grigg 1998, e.g.], however wave energy in these studies is often overly simplified [Storlazzi et al. 2005]. Additionally, whilst surface wave data (such as significant wave height and period) are certainly correlated with the effects of waves on coral [Storlazzi et al. 2005][, this study], the energy surface phenomena are translated to corals through a complex suite of fluid dynamics [Komar 1998, e.g.] that necessitate a deeper analysis. Computer models, in this case Simulating Waves Nearshore (SWAN) [Booij et al. 1999], are well suited for this task because they are by definition composed of such physical equations.

Third generation wave models such as SWAN and WaveWatch III [Tolman 2009] use the spectral action balance equation to track the frequency and direction of waves. Through a combination of statistical wave observations and the two aforementioned variables, all relevant information about waves on the sea can be determined [Holthuijsen 2007]. In the relatively shallow coastal zones where corals exist, additional wave physics (which are not relevant in deep, pelagic waters) come into play, and it was for this reason that SWAN was developed. This makes SWAN perfectly suited to the modeling of wave physics to be applied to coral communities, where small time and spatial scales can create significant changes in the wave field [Holthuijsen 2007]. It is hoped that by running SWAN with high resolution bathymetry and processing the output through the hydrodynamic coral breakage model of Storlazzi et al. [2005], the influence of wave energy on coral populations in the Hawaiian atolls can be better quantified.

For this study, Kure Atoll was selected as a case-study because it had easily available, very high resolution bathymetry, and because it had the greatest climatological range of wave energy [Gove et al. 2011] which should allow for a better assessment of variability in wave conditions. Kure Atoll is located at the northern tip of the Papahanaumokuakea Marine National Monument, more commonly known as the Northwestern Hawaiian Islands (NWHI). Centered at 28°25'N, 178°20'W, Kure is not only the northernmost atoll of the NWHI, but also the northernmost tropical reef atoll in the world [Dana 1971]. While Kure's remote location has spared the atoll's barrier reef from many of the direct effects of anthropogenic activities, Kure bears several reminders of humanity's global reach. Green Island, which is about 86.67 hectares (ha) in area and is located on the southwest corner of Kure, is the only appreciable land mass within the atoll. Green Island supports two permanent man-made structures, a runway and U.S. Coast Guard station, both of which are abandoned and unmaintained [PIBHMC 2011]. As the northernmost atoll in the NWHI, Kure's proximity to the North Pacific Current (the northern component of the North Pacific Gyre) has lead to Kure being speckled with floating debris [Boland et al. 2006]. In addition to these localized anthropogenic influences, global warming has contributed to at least two occurrences of coral bleaching in the past fifteen years [GS et al. 2003; JC and Brainard 2006], an alarming occurrence considering that Kure is the northernmost tropical coral reef ecosystem.

# 2 SWAN Fundamentals

## 2.1 The Action Balance Equation

SWAN is similar to WaveWatch III [Tolman 2009] in that both models solve the (spectral) action balance equation (presented in the style of Holthuijsen [2007] Eq. 9.3.1):

$$\frac{\partial N(\sigma,\theta;x,y,t)}{\partial t}+\frac{\partial c_{g,x}N(\sigma,\theta;x,y,t)}{\partial x}+\frac{\partial c_{g,y}N(\sigma,\theta;x,y,t)}{\partial y}+ \\ \frac{\partial c_{\theta}N(\sigma,\theta;x,y,t)}{\partial \theta}+\frac{\partial c_{\sigma}N(\sigma,\theta;x,y,t)}{\partial \sigma}=\frac{S(\sigma,\theta;x,y,t)}{\sigma} \tag{1}$$

where $N$ is action density, $\sigma$ is the relative frequency, $\theta$ is the propagation direction (normal to the wave crest), $x$ and $y$ are horizontal cartesian coordinates, $t$ is time, and $S$ is the source term, representing the cumulative effects of energy sources and sinks. The semi-colon in $N(\sigma,\theta;x,y,t)$ denotes the fact that action density is a direct function of $\sigma$ and $\theta$ (due to spectral energy balance, see below). Briefly describing the left-hand side of the equation: the first term represents the local (i.e. at that grid point) rate of change in $N$ with time, the second and third terms describe the propagation of $N$ in horizontal space ($c_{g,x}$ and $c_{g,y}$ are the group velocities in the $x$ and $y$ directions, respectively), the fourth term accounts for changes in wave direction with $c_\theta$ as the rate of change of direction with time ($d\theta/dt$), and the fifth term represents changes in wave frequency (i.e. period, $T$). For quick reference, Table 1 contains a brief description of all mathematical symbols used in this document. The rest of this chapter will be dedicated to describing the mathematical and statistical basis for the action balance equation as it is incorporated in SWAN.

Table 1: Variables in this document

| Variable | | | |
|---|---|---|---|
| Symbol | Description | Unit | Source |
| Underbar $\underline{\eta}$ | Random variable | — | ‡ 33 |
| $N$ | Action Density | $m^2$/Hz/rad | ‡ 38 |
| $\omega$ | Radian Frequency | rad/sec | ‡ 123 |
| $\sigma$ | Relative Frequency | rad/sec | ‡ 218 |
| $\theta$ | Wave Propagation Direction | rad | ‡ 43 |
| $c_g$ | Group Velocity | m/s | ‡ 127 |
| $S$ | Generic Action Balance Source/Sink | $m^2$/Hz | ‡ 173 |
| $H$ | Wave Height | m | ‡ 27 |
| $T$ | Wave Period | s | ‡ |
| $L$ | Wave Length | m | ‡ |
| $\eta$ | Sea Surface Elevation | m | ‡ 31 |
| $\alpha$ | Phase (of Harmonic Wave) | rad | ‡ 31 |
| $f$ | Frequency ($1/T$) | Hz | ‡ 31 |
| $\alpha_{wind}$ | Initial Linear Wave Growth Term | ?? | ‡ 290 |
| $\beta_{wind}$ | Non-linear Wave Growth Parameter | ?? | ‡ 290 |
| $S_{in,wind}$ | Source Term, Wind Input | $m^2$/Hz | ‡ 290 |
| $\theta_{wind}$ | Wind Direction | rad | ‡ 290 |
| $u_*$ | Friction Velocity (of wind) | ?? | ‡ 290 |
| $G$ | Low Frequency Growth Cut-Off | ?? | ‡ 290 |
| $\gamma_{Miles}$ | Miles Parameter for Wave Growth | ?? | ‡ 291 |
| $\kappa$ | von Kármán Constant | ND | ‡ 291 |
| $\lambda_{crit}$ | Critical Wave Height | ND | ◇ 1634 |
| $S_{nl4}$ | Source term, quadruplets | $m^2$/Hz/s | ‡ 186 |

- † Booij et al. [1999]
- ‡ Holthuijsen [2007]
- ◇ Janssen [1991]

## 2.2 The Wave Field

From linear wave theory, the height of waves on the sea surface ($\eta$) can be described by the random-phase/amplitude model [Holthuijsen 2007, p.44]. In the idealized, two-dimensional case, varying in time, $\eta$ would be the sum of a large number of harmonic waves. Each wave would have an evenly distributed ($0 < \alpha \leq 2\pi$) random phase, $\alpha$ and a Rayleigh distributed amplitude, $a$. Therefore, at any point and time ($x$, $y$, $t$), $\eta$ (which is a random[1]variable, denoted by the underline: $\underline{\eta}$) is described by (Eq 3.5.20 of) Holthuijsen [2007]:

$$\underline{\eta}(x,y,t) = \sum_{i=1}^{i_{max}} \sum_{j=1}^{j_{max}} \underline{a}_{i,j} \mathrm{cos}(2\pi f_j t - k_i x \mathrm{cos}(\theta_j) - k_i y \mathrm{sin}(\theta_j) + \underline{\alpha}_{i.j}) \tag{2}$$

where $k_i$ is the wave number ($2\pi/L$) of an individual harmonic wave that is traveling in the direction $\theta_j$ with a frequency of $f_i$.

To solve Eq. 2, the range of possible frequencies of ocean waves (0.01–1.0 Hz in open seas [Holthuijsen 2007, p. 34]) is discretized to $j_{max}$ number of frequency bins ($f_j$). Each frequency bin will correspond to a statistically likely amplitude, $a$, and collectively, the expected amplitudes (as a function of frequency) follow a Rayleigh distribution with a high frequency tail (Fig 1).

## 2.3 Generation by wind

At sea, waves are generated by turbulence at the interface between two fluids: the air above and the water below. From a modeling standpoint, the transfer of wind energy to ocean waves is a source term ($S_{in,wind}$) divided into an initial linear growth term ($\alpha_{wind}$), and a more prominent non-linear growth term, which is the product of the current energy density $E$ and a nonlinear parameter $\beta_{wind}$.

$$S_{in,wind}(\sigma,\theta) = \alpha_{wind} + \beta_{wind} E(\sigma,\theta) \tag{3}$$

The linear component of this formulation has been incorporated as a means of empirically generating waves on a smooth ocean surface, and is accredited to Cavaleri and Malanotte-Rizzoli [1981] with a low frequency cut-off modification added by Tolman [1992]:

$$\alpha_{wind} = \begin{cases} \frac{1.5\times10^{-3}}{g^2 2\pi}[u_* cos(\theta - \theta_{wind})]^4 G & \text{for } |\theta - \theta_{wind}| \leq 90^\circ \\ 0 & \text{for } |\theta - \theta_{wind}| > 90^\circ \end{cases} \tag{4}$$

---

[1] In this case, random implies that the variable could not be predicted exactly

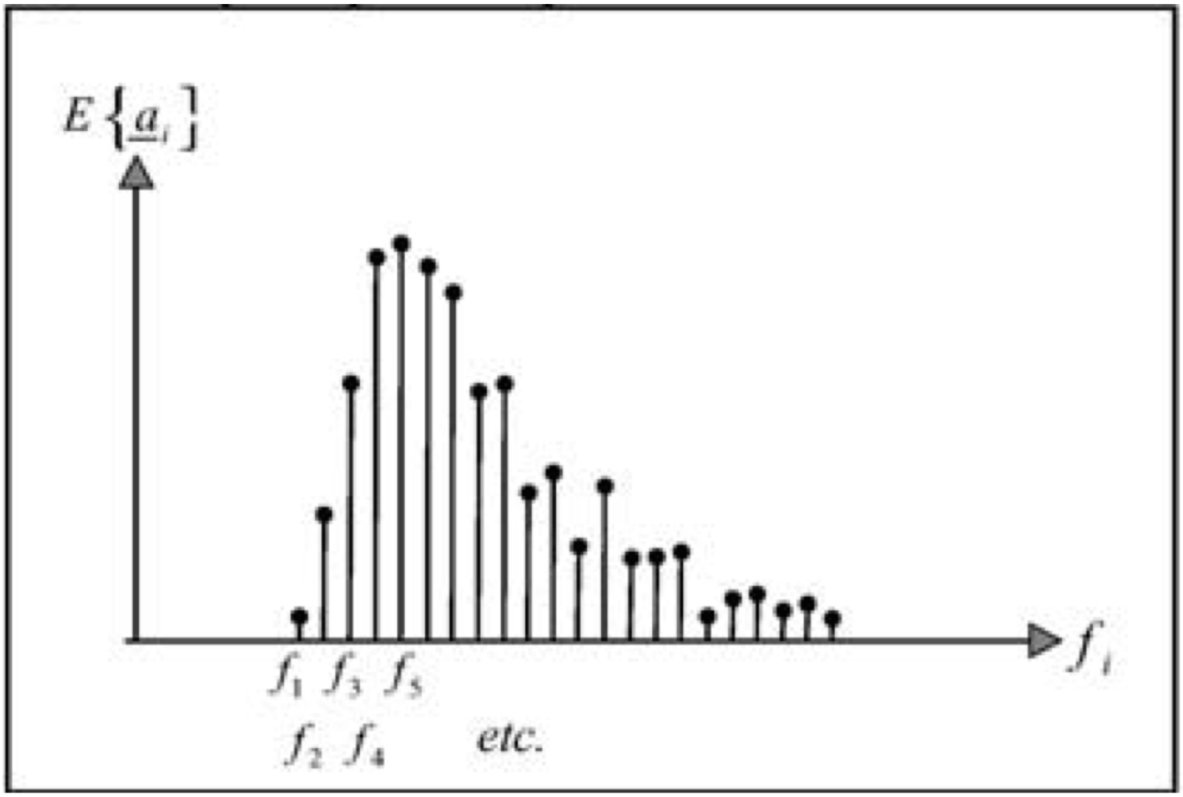

Figure 1: Example Rayleigh distribution of wave amplitude as a function of frequency [Holthuijsen 2007, p.35].

where $u_*$ is the friction velocity of the wind vector (to be discussed below), and $G$ is the Tolman [1992] cut-off function:

$$G = e^{[-(28\sigma u_*/0.26\pi g)^{-4}]} \tag{5}$$

The addition of $G$ is necessary because initial wave growth takes place at high frequencies [Tolman 1992, p.1097], with energy transferred to lower frequencies as the sea state develops [Holthuijsen 2007]. Without the cutoff, energy would be erroneously added to low-frequency waves causing unrealistic spectral distributions.

While initial generation can be an important aspect of idealized test cases, most real-world scenarios will not begin with the sea completely at rest, and the wave field will already be populated by waves from areas anon. In this case, with waves already present, the transfer of energy from the wind to the waves becomes a function of surface pressure at the wind-wave interface. According to Miles [1957], waves distort the flow of the wind above them, causing otherwise horizontal streamlines to follow a profile similar to the sea surface. This in turn causes the wind to exert a greater surface pressure on the windward side of the wave, pushing water particles downward, and a reduced surface pressure on the leeward side, pulling water particles upward [Holthuijsen 2007, p. 179]. The alternating push and pull of the surface pressure transfers additional energy to the wave, causing it to grow in height. Finally, as the wave height increases, the wave can interact with a larger vertical section of the wind, increasing effectiveness of the growth mechanism and creating a non-linear positive-feedback mechanism [Miles 1957].

The Miles feedback mechanism is the primary means of energy transfer from wind to ocean waves. In SWAN, this feedback is accounted for in the second term of Eq 3, where the inclusion of $E(\sigma, \theta)$ (which is the energy density, as derived from the amplitude spectrum, see Fig 1) provides for the dependence on wave height. The parameter $\beta_{wind}$ is calculated following WAM Cycle IV [Komen et al. 1994]:

$$\beta = \max\left\{0, \gamma_{Miles}\frac{\rho_{air}}{\rho_{water}}\left(\frac{u_*}{c}\right)^2 \cos^2(\theta - \theta_{wind}\right\}\sigma \tag{6}$$

wherein the Miles parameter ($\gamma_{Miles}$) has been retuned by Janssen [1991] to better match observations, yielding:

$$\gamma_{Miles} = \frac{1.2}{\kappa^2}\lambda_{crit}\ln^4\lambda_{crit} \tag{7}$$

with the von Kármán constant $\kappa = 0.41$, and the dimensionless 'critical height' ($\lambda_{crit}$) given by [Holthuijsen 2007, p. 291]:

$$\lambda_{crit} = \frac{gz_e}{c^2}\exp[\kappa c/|u_* cos(\theta - \theta_{wind})|] \qquad \text{for } \lambda_{crit} \leq 1 \tag{8}$$

and

$$\beta_{wind} = 0 \qquad \text{for } \lambda_{crit} > 1 \tag{9}$$

In SWAN, equations 6–9 are solved using the relationships established by Janssen [1991]. Procedurally, the iterative approach of Mastenbroek et al. [1993] is used. First, the wave stress ($\tau_{wave}$), which represents the effect of the waves on the wind, is solved for:

$$\tau_{wave} = \rho_{water} \int_0^{2\pi} \int_0^{\inf} \sigma \beta E(\sigma, \theta) d\theta d\sigma \tag{10}$$

using $E(\sigma, \theta)$ from the previous time step. Next, the friction velocity ($u_*$), surface roughness length ($z_0$), effective surface roughness length ($z_e$), and total shear stress ($\tau = \tau_t + \tau_w$, with $\tau_t$ representing turbulence) are found by iterating the following three equations:

$$U_{10} = \frac{u_*}{\kappa} \ln\left(\frac{10 + z_e + z_0}{z_e}\right) \tag{11}$$

$$z_0 = 0.01 \frac{u_*}{g} \tag{12}$$

$$z_e = \frac{z_0}{\sqrt{1 - \tau_{wave}/\tau}} \tag{13}$$

where $U_{10}$ is the user input wind at 10m elevation, $\tau$ is related to $u_*$ via $\tau = \rho_{air} u_*^2$, and Eq 12 is a Charnock-like relation with a constant of 0.01 [SWAN Team 2013a, p. 19].

## 2.4 Nonlinear Wave-Wave Interactions

Nonlinear wave-wave interactions are a type of resonance interaction, and are the primary mechanism of energy transfer between waves. There are two distinct types of nonlinear wave-wave interactions, triads and quadruplets, which describe interactions between 2–3 and 4–5 wave groups, respectively [Holthuijsen 2007]. In the case of triad wave-wave interactions, two wave groups of frequencies $f_1$ and $f_2$, traveling toward each other at directions $\vec{k}_1$ and $\vec{k}_2$ will cross. The diamond pattern formed by the waves and troughs of the crossing groups will form a new wave group with a frequency that satisfies $f_1 + f_2 = f_3$ and a direction that satisfies $\vec{k}_1 + \vec{k}_2 = \vec{k}_3$. Triad wave-wave energy transfers can also occur if a third wave group with frequency $f_3$ and direction $\vec{k}_3$ crosses the diamond pattern formed by wave groups 1 and 2. This phenomena is well illustrated by Figure 6.19 of Holthuijsen [2007]. In either case, the total energy in the system remains constant, and is simply redistributed between the three resulting wave groups.

The primary limitation on triads is that these interactions can only occur in very shallow water, where waves are said to be non-dispersive, and the phase speed ($c_{shallow}$) is a function of gravity ($g$) and depth ($d$) alone, i.e. $c_{shallow} = \sqrt{gd}$. In SWAN, triads can only occur in water shallow enough to meet the previous condition, or in areas where the water is shallow enough for near resonance to occur, in which case energy transfer and phase-coupling affect all three resulting wave components [Holthuijsen 2007, p. 271]. As this paper focuses on wave energy, it is also important to consider how this quantity is handled. The energy transfer between the triad waves depends on the relative magnitudes of the three phases: $\phi_1$, $\phi_2$, and $\phi_1 + \phi_2 = \phi_3$, which are used to compute the biphase ($\beta_{1,2}$):

$$\beta_{1,2} = \phi_1 + \phi_2 - \phi_3 \tag{14}$$

á la Holthuijsen [2007, p. 289]. In very shallow water, waves become saw-toothed and the biphase approaches −90°, which leads to the operational equation

$$\beta_{1,2} = -\frac{\pi}{2} + \frac{\pi}{2}\tanh\left(\frac{\delta_{Ur}}{U_r}\right) \tag{15}$$

[SWAN Team 2013a, p.30], where $U_r$ is the Ursell number, representing the ratio of steepness to relative depth, and $\delta_{Ur}$ is a coefficient that varies within the range of 0.2–0.6 [Holthuijsen 2007, p.274], and is by default set to 0.2 [SWAN Team 2013a, p.30].

$$U_r = \frac{\text{steepness}}{\text{relative depth}} = \frac{g}{8\sqrt{2}\pi^2}\frac{H_s T_{m01}^2}{d^2} \tag{16}$$

with $H_s$ as the significant wave height, and $T_{m01}$ as the ratio of the zeroth and first moment of the variance density spectrum ($\frac{m_{01}}{m_{02}}$). Because the Ursell number represents the degree of nonlinearity of the wave, and because triads are inherently nonlinear, $U_r$ determines whether or not triads take place, and they are only accounted for when $0 \leq U_r \leq 1$ [SWAN Team 2013a, p.30].

To speed up computation time, SWAN uses the 'Lumped Triad Approximation' (LTA) of Eldeberky [1996].

Quadruplets, the second type of wave-wave interaction, can occur in both shallow and deep water, and are largely responsible for wave-wave energy transfer in the latter. Quadruplets form via resonance, in a similar fashion to triads. In this case of quadruplets, instead of two wave components meeting, two *pairs* of wave components must meet, the first pair with frequencies and directions $f_1$, $f_2$, $\vec{k}_1$ and $\vec{k}_2$, and the second pair with frequencies and directions $f_3$, $f_4$, $\vec{k}_3$ and $\vec{k}_4$. When the both pairs cross at the same location (i.e. the diamond patterns are superimposed), $f_1 + f_2 = f_3 + f_4$, and $\vec{k}_1 + \vec{k}_2 = \vec{k}_3 + \vec{k}_4$, resonance, and therefore energy transfer, occurs [Holthuijsen 2007, p. 184]. The source term for quadruplet interactions ($S_{nl4}$) is computed with the Boltzmann integral of Hasselmann [1962], reformatted in terms of energy density by Holthuijsen [2007]:

$$\begin{aligned} S_{nl4}(\vec{k}_4) = &\int\int\int\int T_1(\vec{k}_1, \vec{k}_2, \vec{k}_3) E(\vec{k}_1) E(\vec{k}_2) E(\vec{k}_3) d\vec{k}_1 d\vec{k}_2 \\ &- E(\vec{k}_4) \int\int\int\int T_2(\vec{k}_1, \vec{k}_2, \vec{k}_4) E(\vec{k}_1) E(\vec{k}_2) d\vec{k}_1 d\vec{k}_2 \end{aligned} \tag{17}$$

where $E(f, \theta)$ has been recast in terms of $\vec{k}$, while $T_1$ and $T_2$ are transfer coefficients comprised of the variables $\vec{k}$, $\omega$, and $H$ of the waves involved [Hasselmann 1962, p.497].

# 3 Methods

## 3.1 Wind, Wave and Bathymetry Data

The Kure Atoll bathymetry data in this study were gathered by NOAA and the Pacific Islands Benthic Habitat Mapping Center (PIBHMC) in 2006, and are available from `http://www.soest.hawaii.edu/pibhmc`. The in situ data were gathered using a 30 kHz Simrad EM300 sonar and a 300 kHz SImraid EM3002d sonar aboard the NOAA R/V Hilialakai, and a 240 kHz RESON 8101-ER sonar aboard the NOAA R/V AHI (Acoustic Habitat Investigator) [NOAA 2007]. Sonar data were supplemented by IKONOS satellite imagery from the NOAA/NOS/NCCOS/CCMA[2]Remote Sensing Team, with IKONOS providing all of the data from 0–16 m depths. The final gridded bathymetry was created by dividing the satellite and sonar data into identical grids, and averaging the values where the datasets did not match. According to the authors, the depth data are accurate to within ±1 m.

To prepare the bathymetry data for SWAN, the GMT ('.grd') files were loaded into MATLAB, and missing values were filled in with an average of their closest neighbors. All grid cells surrounding the known Kure bathymetry were set to a constant depth of 1000 m. While this is not realistic, it is unlikely that this simplification will have an impact on surface wind waves [Holthuijsen 2007]. As can be noticed in the Fig 2, the iterative procedure used to fill in the missing values caused 'ridges' to appear on the north, southeast, and southwest corners of the island. The shallowest of these artifacts is around 700m depth, and at this depth it is still unlikely that surface waves will be affected. The resulting bathymetry grid was defined from a depth of 1000m at the edges, to 0m at the barrier reef encircling the island, the only missing values (which will be interpreted as land in

---

[2] NOS: National Ocean Service, NCCOS: National Center for Coastal Ocean Science, CCMA: Center for Coastal Monitoring and Assessment

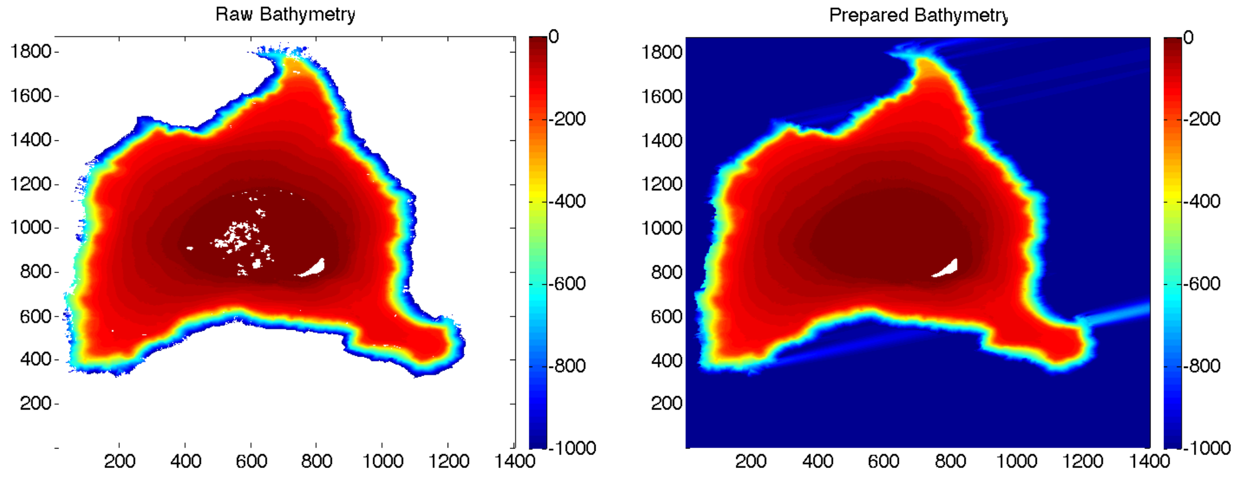

(a) Raw bathymetry data from PIBHMC.

(b) Bathymetry data that were fed into SWAN for modeling simulations.

Figure 2: Visual comparison of the raw bathymetry data **(a)** and the bathymetry data used by SWAN **(b)** which has had all missing values filled. Green Island is left as missing data points, which SWAN interprets as land.

SWAN) were the cells defining Green island. This grid was then saved as an ascii file to be read by SWAN.

The wind and boundary wave data are provided by WaveWatch III [Tolman 2002] version 2.22, and are freely available at `http://polar.ncep.noaa.gov/waves/download.shtml?`. Hindcast data at a global spatial resolution of 0.5°are available from February, 2005 to December, 2013, with a temporal resolution of 3 hours. For the present study, hindcast data are especially useful because the data and model are adjusted to best match observations, providing more realistic statistics. To estimate the recent trends in wind and wave activity around Kure, MATLAB was used to extract wind and wave data from the WWIII dataset at the nearest grid point, located at 178°30' W, 28°30' N. A daily mean was attained by averaging (less the missing values) the 3-hour intervals.

Wave data provided were significant wave height ($H_{sig}$), propagation direction ($\theta$), and peak period ($T_p$). Wind data were available as $U_{wind}$ and $V_{wind}$ horizontal vector components. To facilitate the sorting of these data, the direction (in SWAN convention, measured in degrees counter-clockwise (CCW) from the positive x axis) was computed using the arctangent function and the sign of the vectors (to determine the quadrant):

$$\theta_{wind} = \begin{cases} \arctan(V_{wind}/U_{wind}) & \text{if } U \text{ ¿ } 0 \text{ and } V \text{ ¿ } 0 \\ \arctan(V_{wind}/U_{wind} + 180^\circ & \text{if } U \text{ ¡ } 0 \text{ and } V \text{ ¿ } 0 \text{ or } U \text{ ¡}0 \text{ and } V \text{ ¡ } 0 \\ \arctan(V_{wind}/U_{wind} + 360^\circ & \text{if } U \text{ ¿ } 0 \text{ and } V \text{ ¡ } 0 \end{cases} \tag{18}$$

The magnitude of the wind vector was computed using the Pythagorean theorem. Data were sorted into discrete bins containing a range of values. Wind and wave propagation directions were sorted into 10° bins ranging in total from 0° to 360°. Significant wave height was sorted into 1m interval bins (i.e. $0 \leq H_{sig} < 1$, $1 \leq H_{sig} < 2 \ldots H_{sig} \geq 10$), with the final bin containing all occurrences of significant wave heights greater than (or equal to) ten. Wind magnitudes were similarly sorted, with the exception that the range covered 0–20 m/s. Wave periods were sorted into two second interval bins ranging from 0 to 18 s. From the bin data, the top four ranges for each parameter were determined, and run in various combinations to assess both the influence of the individual components as well as the long term average wave energy. Additionally, three 'extreme' event scenarios were run in order to assess the upper climatological limits of expected wave energy. The input parameters were, in this case, found by manually selecting the two largest wave events in the two most common directional octants: NW ($\tilde{3}00^\circ$) and SE ($\tilde{1}00^\circ$)

## 3.2 SWAN Model Setup

The SWAN computational grid covered the entire area of the original Kure atoll bathymetry, divided into 100m×100m cells numbering 280 in the $x$ direction and 373 in the $y$ direction. In the wave spectral space, the frequency range used was $f_{low}$=0.01 to $f_{high}$=1.0. These data were discretized into 49 spectral bins according to the following equation [SWAN Team 2013b]:

$$\text{number of bins} = \frac{\log(f_{low}/f_{high}}{\log(1+\Delta f/f)} \tag{19}$$

in order to comply with the relationship of $\Delta f/f = 0.1$, which is required for the DIA quadruplet approximation. Directional space encompassed 360°, and was discretized into 2° increments (180 bins total). Uniformly distributed wind forcing was applied as a constant across the entire grid, with the magnitude and direction determined by the aforementioned sorting procedure. Wave forcing was fed from two of the four grid sides, as determined by direction of propagation. For example, waves of $\theta = 120°$ (traveling NW) would enter from the south and east borders. For each scenario, a 'stationary' computation was done, largely in order to reduce the overhead associated with a time-stepping process. In essence, a stationary computation solves Eq 1 with the first term equal to zero ($\partial N(\sigma, \theta; x, y, t)/\partial t = 0$).

SWAN allows the user to adjust many parameters in order to accommodate a wide range of uses, some of these options were tailored for this study, as will be discussed below. The user-defined baseline whence the depth is measured was set to the height of the highest fringing reefs of the bathymetry file (0.0m), representing the water level of a completely flat sea surface. The minimum depth, above which waves are forced to break, was set to 0.05m. The wind information fed to SWAN is assumed to be the wind velocity at 10m elevation ($U_{10}$), and these data are converted to the friction velocity $u_*$ using the wind-drag coefficient $C_D$ [SWAN Team 2013a] via the relationship:

$$u_* = U_{10} C_D \tag{20}$$

In order to prevent overestimation of $C_D$ under high wind conditions [Zijlema et al. 2012], a cap of $2.5\times10^{-3}$ is suggested by the SWAN team, and has been implemented for this study. Boundary waves were fitted to the JONSWAP spectrum, with a (default) peak enhancement parameter of $\gamma_{peak} = 3.3$. As dictated by the WWIII data, the input period was the peak period $T_{peak}$ (as opposed to the other commonly used period, the mean period $T_{m01}$). Because the WWIII wave directions were so irregular (see next chapter), a high degree of directional distribution (37.5°) was given for the incoming wave data, in the hopes that this would better approximate the random nature of surface waves. In SWAN, bottom friction accounts for some energy dissipation and is an important aspect of modeling wave energy. The JONSWAP formulations of Hasselmann et al. [1973] are used to account for friction, where the friction coefficient ($C_{fric}$) is a constant 0.038 $\mathrm{m}^2/\mathrm{s}^3$. The value was picked because swell is the dominant form of energy input into the grid, and SWAN Team [2013b] suggested this value for those conditions. As a note however, the choice of $C_{fric} = 0.038$ conflicts with the SWAN model practice of using a higher $C_{fdic}$ value (0.067 $\mathrm{m}^2/\mathrm{s}^3$) for directional distributions above 30°. Despite the rather coarse model resolutions, the attempt was made to include triad interactions (using the LTA method) with the standard SWAN parameter values. Diffraction, however, was disabled, largely because the SWAN authors suggested that a resolution of 10–20% of the dominant wavelength be used for any diffracting obstacle, an impossibility at the 100m resolution of the current model. The parameter that controls the centrality of the refraction scheme (with 0 being fully central, and 1 being a first order upwind scheme) was left at the default value of 0.5; this option provides a balance between the accuracy and instability of a fully central scheme, and the stability and diffusivity of a fully upwind scheme. Finally, the turning rates in spectral space $c_\theta$ and $c_\sigma$ (with $\sigma$ as the relative frequency) are both limited to the upper Courant-Friedrichs-Lewy (CFL) value of 0.5, as suggested by SWAN Team [2013b].

### 3.3 Coral Breakage

Probability of coral breaking was estimated using the methodology of Storlazzi et al. [2005] and Massel [2013]. In this manner, a coral head is assumed to be an idealized cylinder, with height $h_{cor}$, radius $r_{cor}$, and basal radius $r_{cbase}$ (see Table 6). The total pressure applied to the coral is a sum of four forces: lift $F_{cl}$, drag $F_{cd}$, weight $F_{cg}$ and the internal force, $F_{ci}$. The lifting force is caused by the acceleration of water as it flows over the coal head, and is calculated as [Storlazzi et al. 2005, Eq 3]:

$$F_{cl} = \frac{1}{2}\rho C_{lift} u_{bot}^{2} 2 r_{cor} h_{cor} \beta_{hide} \tag{21}$$

where $C_{lift} = 15$ is the lift coefficient for a cylindrical shape [Hoerner 1965], and $\beta_{hide}$ is a hiding parameter that allows the user to fine-tune the density of coral cover, with $\beta_{hide} = 0$ being completely hidden by other corals and $\beta_{hide} = 1$ being completely exposed. Following Storlazzi et al. [2005], $\beta_{hide}$ is set to 0.9, however the authors of that paper state that this choice is somewhat arbitrary. Note that where Storlazzi et al. [2005] uses the average of several near-bed wave orbital velocities in their formulations ($\bar{u}$ in their notation), this study uses the maximum bottom wave orbital velocity, $u_{bot}$ as is output by SWAN. The drag force acting on the coral is simply:

$$F_{cd} = \frac{1}{2}\rho C_{cdrag} u_{bot}^{2} 2 r_{cor} h_{cor} \beta \tag{22}$$

with $C_{cdrag} = 0.85$, chosen by Storlazzi et al. [2005] due to measurements by Denny [1988] and Denny [1993] and Gerhart et al. [1993]. The gravitational force (i.e. the relative weight of the coral in seawater) is a function of volume ($\pi r_{cor}^{2} h_{cor}$) and the relative density:

$$F_{cg} = \left(\rho_{cor} - \rho\right) g \pi r_{cor}^{2} h_{cor} \tag{23}$$

Table 2: Replication of Table 1 in Storlazzi et al. [2005], displaying coral morphological data and mechanical strengths. Coral measurements were gathered by Storlazzi et al. [2005], and mechanical strengths are from Rodgers et al. [2002].

| Coral Species | $h_{cor}$ (m) | $r_{cor}$ (m) | $r_{cbase}$ (m) | $\sigma_{resisti}$ (MPa) |
|---|---|---|---|---|
| *Montipora capitata* | 0.20 | 0.10 | 0.06 | 3.5 |
| *Porites compressa* | 0.15 | 0.02 | 0.02 | 5.3 |
| *Porites lobata* | 1.00 | 0.50 | 0.45 | 6.2 |
| *Pocillapora meandrina* | 0.20 | 0.13 | 0.07 | 7.0 |

where $\rho_{cor} = 1450\text{kg/m}^3$ is the coral skeletal density [Lough and Barnes 1992]. The final force considered, the inertial force, is due to the oscillatory flow of the passing wave causing acceleration and deceleration of the fluid around the coral head. The inertial force is computed via

$$F_{ci} = \frac{51}{24}\rho\pi r_{cor}^2 h_{cor} a_{fluid} \tag{24}$$

where $a_{fluid}$ is reported by Storlazzi et al. [2005] as being “a function of $u_{bot}$ and $T$”, but is not otherwise absolutely defined.

To seek out the equation for $a_{fluid}$, the source of the formulations used by Storlazzi et al. [2005], (i.e. Massel [2013]) was consulted. Massel [2013] reports the inertial force as being the summation of two components ($F_{ci} = F_{ci_1} + F_{ci_2}$), the first being the product of the coral mass and $a_{fluid}$:

$$F_{ci_1} = \rho V_{cor} a_{fluid} \tag{25}$$

and the second being due to the mass of the coral. This second component is derived from the formulation by Milne-Thompson [1960] for kinetic energy ($K_{Es}$) acting on a sphere[3]:

$$K_{Es} = \frac{pi}{3}\rho\left(\frac{D_{ex}}{2}\right)^3\left(1 + \frac{3}{16}\frac{\left(\frac{D_{ex}}{2}\right)^3}{h_{ex}}\right)u_{bot}^2 \tag{26}$$

where $D_{ex}$ and $h_{ex} = \frac{D_{ex}}{2}$ are coral diameter and height from sea floor, respectively, and the subscript ‘*ex*’ denotes that these are merely included to complete the example. Following Kochin et al. [1963],

---

[3] The shape considered in Eq 26 is irrelevant because the equation is only included to illustrate the derivation of $a_{fluid}$ used in this study.

the kinetic energy is converted to the second force component by taking the partial derivatives, first with respect to $u_{bot}$:

$$\frac{\partial K_{Es}}{\partial u_{bot}} = \frac{19}{24}\pi\rho r_{cor}^3 u_{bot} \tag{27}$$

and then with respect to time ($t$):

$$\frac{\partial^2 K_{Es}}{\partial u_{bot}\partial t} = \frac{19}{24}\pi\rho r_{cor}^3 a_{fluid} \tag{28}$$

where $\frac{D}{2}$ has been replaced with $r_{cor}$. The key piece of information from Eqs 26–28 is that $a_{fluid}$ is found by taking the derivative of $u_{bot}$ with respect to time, implying that $a_{fluid}$ is simply:

$$a_{fluid} = \frac{u_{bot}}{T/2} \tag{29}$$

where the period ($T$) is halved because the acceleration only occurs for the first half of the waves passing. Another difference between this study and Storlazzi et al. [2005] is that the authors used the peak period $T = T_p$, and this study uses the mean period $T = T_{m01}$.

The horizontal forces $F_{ci}$ and $F_{cd}$ act above the coral base and create an overturning moment about the neutral axis of the coral, lifting the upstream edge and forcing down on the downstream edge [Massel 2013]. The duality of this creates tension on the upstream edge and compression on the downstream edge, and will cause the coral to fail if either stress is greater than the corresponding (tensile or compressional, respectively) mechanical strength of the coral. Thus, the stress on the coral structure per unit area ($\sigma_{applied}$) is the greater of:

$$\sigma_{applied} = \frac{F_{cg} + F_{cl}}{\pi r_{cbase}^2} \pm \frac{\frac{1}{2}(F_{ci} + F_{cd})2r_{cor}r_{cbase}}{\frac{1}{4}\pi r_{cbase}^4} \tag{30}$$

wherein the denominator of the second term on the RHS is the second order moment of the basal area [Massel 2013]. The combination of forces $F_{cg}$ and $F_{cl}$ in the first term on the right-hand side (RHS) of Eq 30 is due to the fact that these two forces act in the vertical plane, whereas $F_{ci}$ and $F_{cd}$ act in the horizontal, as previously mentioned.

Corals are brittle and fail with negligible deformation, negating the need for considerations where the coral bends but does not break [Storlazzi et al. 2005]. Again following Storlazzi et al. [2005], once the larger $\sigma_{applied}$ value has been taken from Eq 30, it is compared with the species-specific resistive force per unit area ($\sigma_{resist}$) to create a 'Factor of Safety' ($F_{safety}$):

$$F_{safety} = \frac{\sigma_{resist}}{\sigma_{applied}} \tag{31}$$

The values for $\sigma_{resist}$ were calculated by Rodgers et al. [2002], and can be found herein in Table 6. Using this simple metric, corals will be very likely to break when $F_{safety} \leq 1$, because at that point the applied stress is greater than the mechanical strength of the coral.

## 3.4 Coral Spatial Distributions

It is quite fortunate that the main Hawaiian Islands and their distant ancestor Kure share many of the same corals, because this allowed the morphological coral data of Storlazzi et al. [2005] to be used to estimate coral breakage at Kure Atoll. Coral species distributions were provided by Kenyon et al. [2008], who in 2000, 2002 and 2003 conducted coral cover surveys using a combination of video-recorded transects, experienced towed divers, and still photoquadrats. The coral data of Kenyon et al. [2008] are available only for depths above 20m, however, $u_{bot}$ decreases very quickly with depth, and the the upper 20m are the depths most likely to be afflicted by wave-induced coral breaking [Storlazzi et al. 2005]. The towed-diver surveys of Kenyon et al. [2008] were spatially separated around the fore- and back-reef of the atoll, and were therefore quite suited for use in this study. Additionally, towed-diver surveys are reported by the author to be more reliable than the other methods, due to the fact that divers are able to survey a much wider area.

To compare the $F_{safety}$ values from the coral breakage model with the coral spatial information, the grid files for $u_{bot}$ and $T_{m01}$ that were output by SWAN were first loaded into MATLAB. Then, Eq 21–24, 30 and 31 were applied (in that order) for each cell across the grid. Next, $F_{safety}$ values for grid cells corresponding to depth ranges reported by Kenyon et al. [2008] were analyzed for three areas: the fore-reef (depths: 10–20m), the back-reef (depths: 0–5m[4]), and the lagoon, which was only analyzed in one area which corresponds to the study site in Fig. 2 of Kenyon et al. [2008]. All grid cells of $F_{safety}$ that did not correspond to a depth of the appropriate range were removed (set to NaN) and the resulting matrices were visually analyzed using colored plots to determine ranges and spatial variability of $F_{safety}$.

---

[4] While Kenyon et al. [2008] reports only examining depths of 0.7–1.4m in their study, this range was expanded to include more grid points in the model data.

# 4 Results

## 4.1 Boundary Conditions

WaveWatch III data were available from February 2005 to December 2013, and time-series and sorted bins (as per the process described in Chapter 3.1) are displayed in Figs. 3–5. Wind direction ($\theta_{wind}$) time-series data (first plot, Fig 3) ranged from 10–350°, and featured greater variability in the northern hemisphere winters. Statistically, the $\theta_{wind}$ data featured a mean of $\tilde{1}70°$, and the top four 10° bins were: 190–200°, 180–190°, 200–210°and 170–180° in that order (second plot, Fig 3, Table 3). The hourly $\theta_{wind}$ data were available in three hour intervals, and were used to compute a daily average of eight values. The daily standard deviation of this averaging process ranged from $\tilde{0}$–188°, with an average of 36°and 62% of calculated deviations were below 20°. Additionally, standard deviations for $\theta_{wind}$ were often greater during periods of greater wind variability.

Wind magnitudes ranged from 1–20 m/s (rounded to closest integer), with an average of 6.9 m/s. The wind magnitude data highlighted a consistent trend of greater magnitudes during the Kure winter, with strongest annual winds always appearing during winter months, with one exception in 2012. (third plot, Fig 3). After sorting into 1 m/s bins, the top four wind magnitude bins were: 5–6, 6–7, 7–8 and 8–9 m/s, in that order (fourth plot, Fig 3, Table 3). The daily standard deviations values for wind magnitude data ranged from $\tilde{0}$ to $\tilde{6}$ m/s, with an average of 1.2 m/s, and with 75% of all values below 1.5 m/s (64% of values between 0.5 and 1.5). And finally, showing a similar temporal pattern to wind direction, the standard deviation values for wind magnitude were greater during periods of stronger wind activity (i.e. Kure winters).

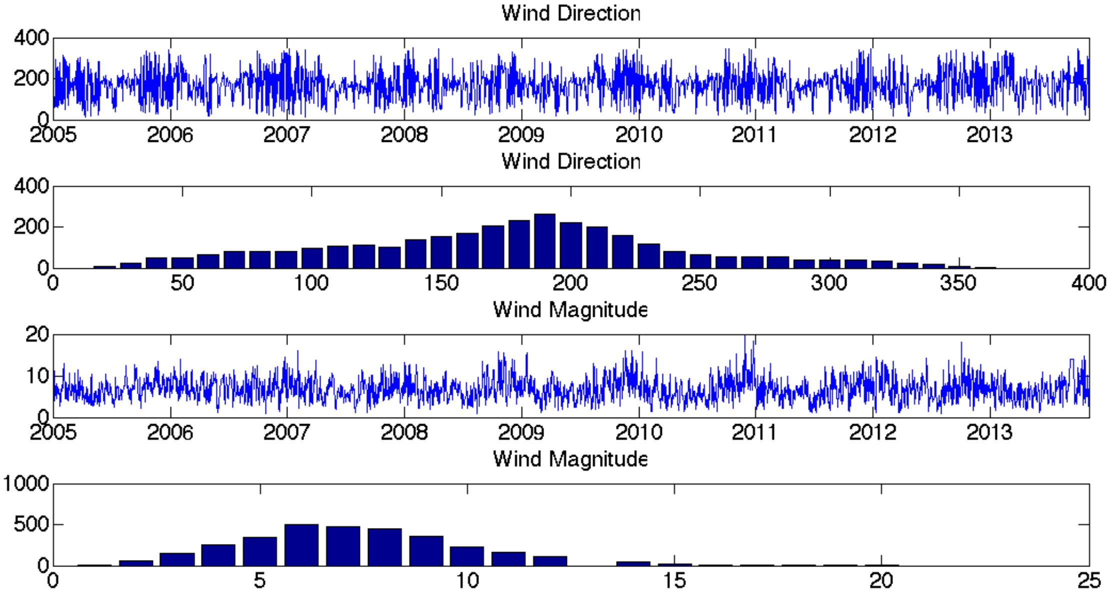

Figure 3: Daily wind data at 178.5°W,28.5°N., averaged from 3-hourly output from WWIII. Top plot is wind direction in degrees CCW from due east. Second plot is the daily data from the top plot sorted into 10° directional bins ranging from 0–360°. The third plot is a time series of wind magnitude in m/s. The fourth plot is the wind magnitude data from the third plot, sorted into 1m bins.

Significant wave heights displayed a strong seasonal signal, rising in the fall and peaking in early winter (first plot, Fig 4). Wave heights ranged from 0.7–9.2[5] m, with an average of 2.6 m. The top significant wave height bin, 0–1 m, contained 36.85% of all values, the next three largest bins were: 2–3 m, 3–4 m and 4–5 m (second plot, Fig 4, Table 3). Standard deviations for the significant wave height were highest during the periods of high wave activity (i.e. fall/winter) and ranged from 0 to 2 m, with 94.8% of values between 0 and 0.32 m.

Peak period ($T_p$) ranged from 4 to 17.6 s, with a mean of 10.2 s. Peak period also tracked temporally with significant wave height, rising above 10 s in the winters and dipping below 10 s in the summers (third plot, Fig 4). Standard deviations for daily $T_p$ averages showed a fairly noisy

---

[5] This value was used for an 'extreme event' analysis

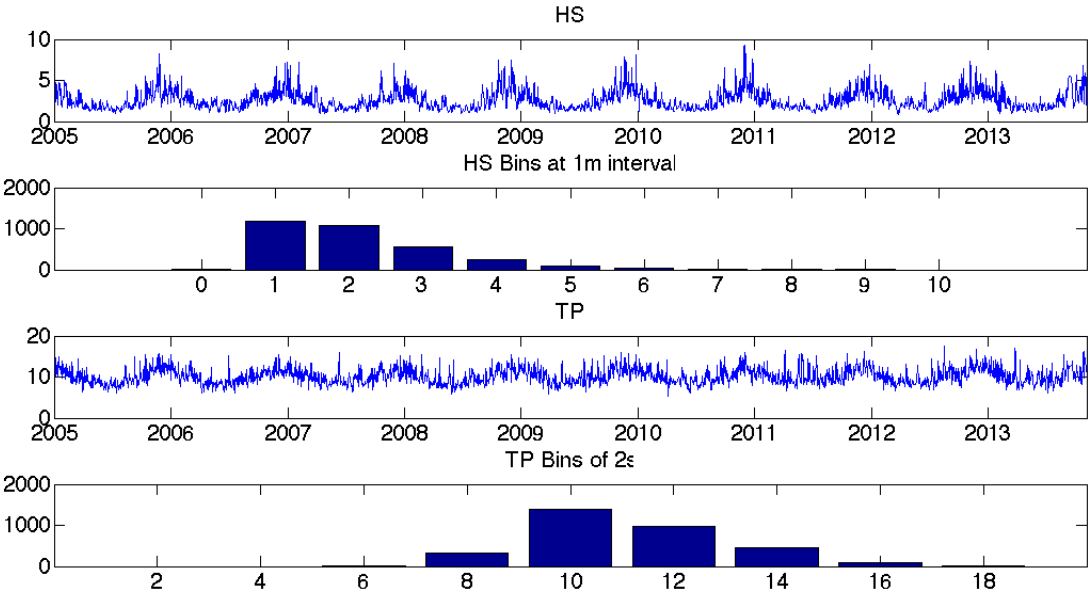

Figure 4: Daily wave $H_{sig}$ $T_{peak}$ data at 178.5°W,28.5°N., averaged from 3-hourly output from WWIII. The top plot shows $H_{sig}$ in m. The second plot displays the $H_{sig}$ data from the top plot, sorted into 1m bins. The third plot shows $T_{peak}$ in seconds. The fourth plot shows the data from the third plot, separated into 2s bins.

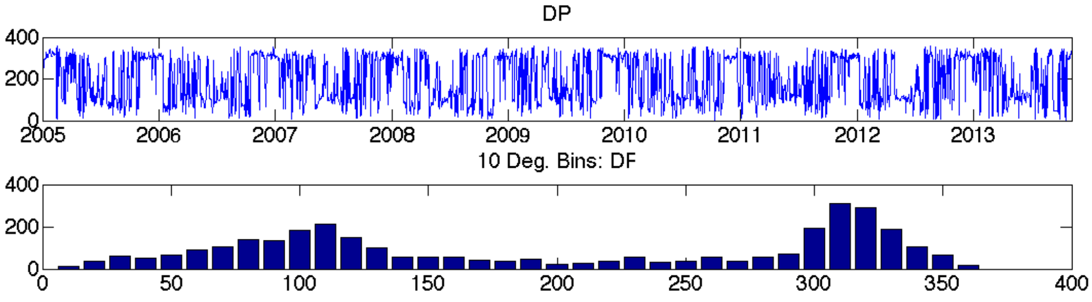

Figure 5: Daily wave propagation direction data at 178.5°W,28.5°N., averaged from 3-hourly output from WWIII. The top plot shows the direction of wave propagation ($\theta$) measured CCW from due east. The second plot shows the data from the top plot, sorted into 10° bins.

Table 3: Four most common conditions for wind and wave forcing data from WWIII, as dictated by the sorting displayed in Figs 3–5

| Rank | | Waves | | Winds | |
|---|---|---|---|---|---|
| | $H_{sig}$ | $T_{m01}$ | $\theta$ | Mag. | $\theta_{wind}$ |
| 1 | 1–2 | 8–10 | 300–310 | 5–6 | 190–200 |
| 2 | 2–3 | 10–12 | 310–320 | 6–7 | 180–190 |
| 3 | 3–4 | 12–14 | 100–110 | 7–8 | 200–210 |
| 4 | 4–5 | 6–8 | 290–300 | 8–9 | 170–180 |

time-series with peaks throughout the year. The standard deviations ranged from 0–5.6 s with an average of 0.64 s, and 90.7% of data points below 1.6 s. Sorting into 2 s bins showed that 42.7% of $T_p$ values fell within the range of 8 to 10 s (the largest bin), with bins for 10–12 s, 12–14 s, and 6–8 s ranking second, third, and fourth, respectively.

Wave directions ($\theta$) spanned nearly the entire directional space (3–358°) as measured CCW from due East (the positive $x$ axis). Time-series data showed wave directions without a strong seasonal signal, however there was a tendency toward northwesterly waves (300–330°) during the northern hemisphere fall (first plot, Fig 5). Standard deviations for wave direction ranged from 0–189°with 63% of values below 10.5°(the mean was 30°). Temporal evaluation of the standard deviation revealed that the signal was consistently noisy, often spiking between 0 and 100°+. Sorting into 10°bins showed a dual-peaked distribution, with the larger peak (27.8% of data points) between 290 and 320°, and the smaller peak (16.7% of data points) between 90 and 120°(second plot, Fig 5). The top four bins for wave direction were: 300–310°, 310–320°, 100–110°and 290–300°(Table 3).

The four largest bins for each boundary variable were used to simulate the statistically likely wave conditions around Kure Atoll, as well as to assess the influence of each parameter on $F_{safety}$. In general, the strategy with model trials was to set all parameters equal to the values of the top ranked bins (i.e. the ‘Most Common Conditions’, or MCC) and then to vary one boundary condition

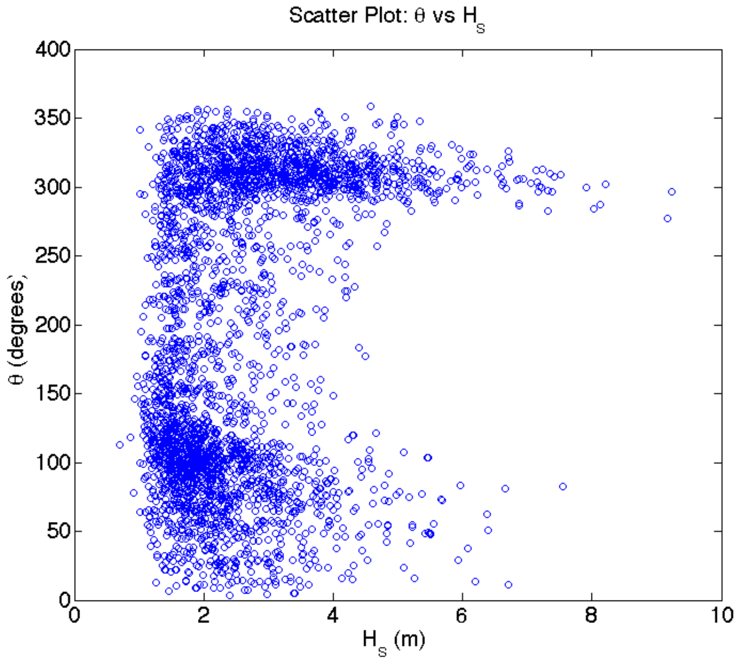

Figure 6: Scatter plot of $\theta$ vs $H_{sig}$, as derived from the daily WWIII data.

through the four possible values (Table 4). Once it was seen that significant wave height had the greatest influence on $F_{safety}$, all four $H_{sig}$ values were evaluated for conditions with southeasterly swell (100–110°). In addition to the statistically likely bin data used to simulate the most common conditions, three extreme events were analyzed to determine the potential threat to Kure's coral communities. Two of the extreme events selected were significant wave height based, one trial for each of the primary wave directional sectors ($\tilde{3}$00°and $\tilde{1}$00°). The two trials featured the highest $H_{sig}$ in each sector: 9.2 m approaching from the northwest, and 7.5 m approaching from south-southeast (Fig 6). The third trial was selected based on peak period, for which the highest daily $T_p$ value (17.6 s) was selected. For extreme conditions, all other boundary data were taken from the day corresponding to the selected values, (as opposed to using the statistically likely data) and all boundary data can be found in Table 4.

Table 4: Boundary Conditions, Forcings, and Trial Types

| Trial Info | | Waves | | | Wind | |
|---|---|---|---|---|---|---|
| Trial | Flag | $H_{sig}$ | $T_p$ | $\theta$ | Mag. | $\theta_{wind}$ |
| 1 | | 1.5 | 9 | 305 | 5.5 | 195 |
| 2 | | 1.5 | 9 | 305 | 8.5 | 195 |
| 3 | | 1.5 | 9 | 295 | 5.5 | 195 |
| 4 | | 1.5 | 9 | 305 | 5.5 | 185 |
| 5 | | 1.5 | 9 | 305 | 8.5 | 195 |
| 6 | | 1.5 | 9 | 305 | 7.5 | 195 |
| 7 | | 1.5 | 9 | 305 | 6.5 | 195 |
| 8 | | 2.5 | 9 | 305 | 5.5 | 195 |
| 9 | | 3.5 | 9 | 305 | 5.5 | 195 |
| 10 | | 4.5 | 9 | 305 | 5.5 | 195 |
| 11 | | 1.5 | 11 | 305 | 5.5 | 195 |
| 12 | | 1.5 | 13 | 305 | 5.5 | 195 |
| 13 | | 1.5 | 7 | 305 | 5.5 | 195 |
| 14 | | 1.5 | 9 | 305 | 5.5 | 205 |
| 15 | | 1.5 | 9 | 305 | 5.5 | 175 |
| 16 | | 1.5 | 9 | 315 | 5.5 | 195 |
| 17 | SE | 1.5 | 9 | 105 | 5.5 | 195 |
| 18 | SE | 2.5 | 9 | 105 | 5.5 | 195 |
| 19 | SE | 3.5 | 9 | 105 | 5.5 | 195 |
| 20 | SE | 4.5 | 9 | 105 | 5.5 | 195 |
| 21 | SE | 1.5 | 11 | 105 | 5.5 | 195 |
| 22 | EX | 9.2 | 16 | 296 | 13.5 | 139 |
| 23 | EX | 7.5 | 11.4 | 83 | 18.3 | 200 |
| 24 | EX | 3.4 | 17.6 | 319 | 8.1 | 204 |
| 25 | TST | 1.5 | 9 | 305 | 5.5 | 195 |

## 4.2 Model Results & Coral Safety

The first trial was run using the ‘most common conditions’ (MCC), i.e. the top bins for all boundary parameters (Rank 1, Table 3). Under the combination of the most statistically likely wave and wind conditions, $u_{bot}$ (at depths of 10–20 m) ranged from 0 to 0.4 m/s (Fig. 7). Spatially, $u_{bot}$ values were higher on the NW quadrant that faced the incoming boundary conditions, and lowest on the opposite side (Fig 7a), a trend which all trials followed. The average period ranged from 7.3 s in the NW quadrant down to $\tilde{4}$ s at the SE corner of the atoll, and the highest $T_p$ values were

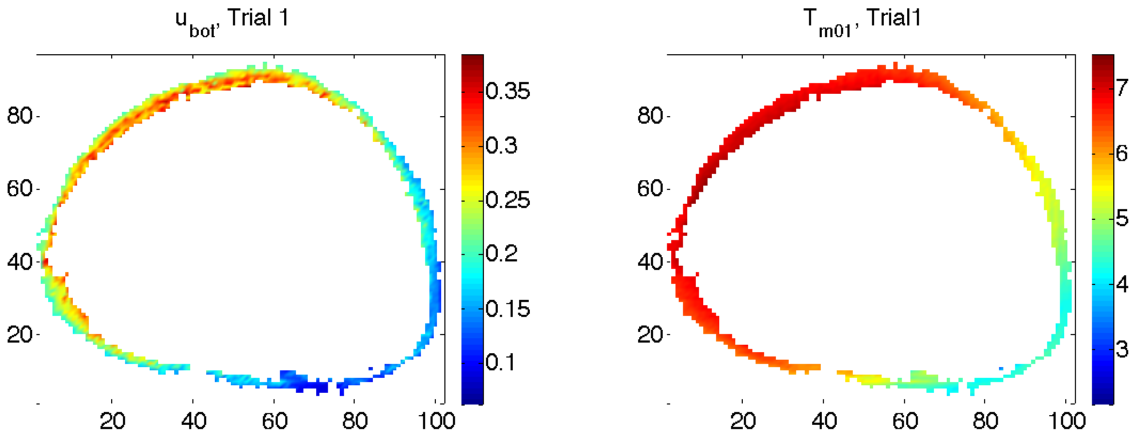

(a) SWAN modeled $u_{bot}$, trial 1, depths: 10–20 m. (b) SWAN modeled $T_{m01}$, trial 1, depths: 10–20 m.

Figure 7: Trial 1 using MCC: $H_{sig} = 1.5$ m, $T_p = 9$ s, $\theta = 310°$, wind magnitude $= 5.5$ m/s and $\theta_{wind} = 195°$. These plots are for fore-reef analysis, and all cells corresponding to depths outside the range of 10–20m have been removed.

not always located with the highest $u_{bot}$ values (Fig 7). Determining the species-specific $F_{safety}$ values required application of Eq 30, which features a '±' symbol to denote that either tensional or compressional force may cause a coral to fracture. Preliminary results showed that when using Eq 30 with a difference operator, the $\sigma_{applied}$ values would take on unrealistic negative values. Thus, for all $F_{safety}$ calculations, $\sigma_{applied}$ is computed via Eq 30 where the ± symbol has been replaced with a +. For Trial 1, $F_{safety}$ values on the order of $10^2$–$10^3$ were calculated, with 400–1400 for *M. capitata*, 800–2200 for *P. meandrina*, 975–1150 for *P. lobata*, and 1000–6000 for *P. compressa* (Table 5)

Changes in wind direction (Trials 1, 4, 14 15), did not cause large variations in $u_{bot}$, $T_p$, or $F_{safety}$ values (Table 5). The average period ranges for trials 4, 14 and 15 were 4–7, 4.5–7 and 4–7.25 s (respectively) all of which are within the MCC range of 4–7.3 s. Similarly, these three non-MCC trials (4, 14 and 15) had a $u_{bot}$ range of 0.1–0.35 m/s, within the MCC range of 0–0.4 m/s. Factor of safety ranges for all four coral species were fairly consistent (Table 5), and all ranges were within 100 (200 in the case of *P. compressa*) units of one another. Also for all coral species,

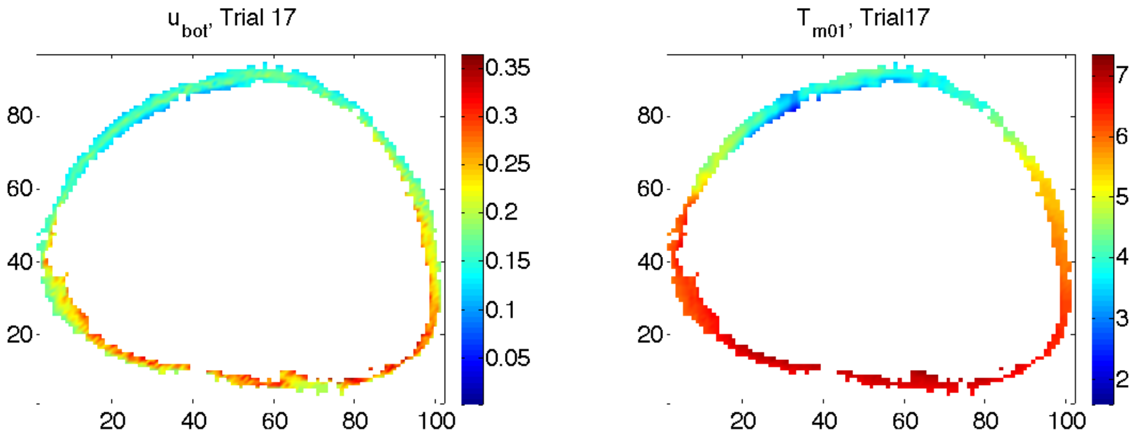

(a) SWAN modeled $u_{bot}$, Trial 17, depths: 10–20 m. (b) SWAN modeled $T_{m01}$, Trial 17, depths: 10–20 m.

Figure 8: Trial 17 using MCC: $H_{sig} = 1.5$ m, $T_p = 9$ s, wind magnitude = 5.5 m/s and $\theta_{wind} = 195°$, and direction of wave propagation of 105°(measured CCW from due east). These plots are for fore-reef analysis, and all cells corresponding to depths outside the range of 10–20m have been removed.

each of the southeasterly wave non-MCC trials (17–21) shows slightly higher $F_{safety}$ values than does the MCC trial.

Wind magnitude trials were run for constant wind speeds of 5.5 (MCC), 6.5, 7.5 and 8.5 m/s with the latter three corresponding to trials 7, 6 and 5 respectively (Table 5). Like wind direction, all three non-MCC wind magnitude trials had $u_{bot}$ ranges of 0.1–0.35 m/s. Average period ranges were 3.5–6 (trial 5) and 3.5–7 (trials 6 and 7), slightly less than the MCC range (4–7.3 m/s). Factor of safety ranges for *P. lobata* and *P. compress* were identical for all three non-MCC runs, and differed by only 100 units for *P. meandrina* and *M. capitata.*

The common peak periods used to drive the model were 9 s (MCC), 11 s (Trial 11), 13 s (Trial 12) and 7 s (Trial 13). Greater periods at the boundaries did cause an increase in ranges of $u_{bot}$ and $T_{m01}$ (Table 5). In order of increasing period, trials 13, 1, 11 and 12 featured $u_{bot}$ ranges of 0.05–0.3, 0–0.4, 0.1–0.45 and 0.15–0.45 (respectively). Mean period ranges saw a similar trend, increasing with each 2s increase in period. The changes in wave energy brought in by boundary

Table 5: Model Results, All Trials: $u_{bot}$, $T_p$ and $F_{safety}$ Values for the Fore-reef (10–20m)

| Trial Info | Model Data | | Coral $F_{safety}$ | | | | |
|---|---|---|---|---|---|---|---|
| Number | Type | $u_{bot}$ | $T_{m01}$ | *P. meandrina* | *P. lobata* | *M. capitata* | *P. compressa* |
| 1 | MCC | 0–0.4 | 4–7.3 | 900-2200 | 975–1150 | 500–1400 | 1000-6000 |
| 2 | Wind Mag. | 0.1–0.35 | 3.5–6.5 | 1000-2200 | 975–1200 | 600–1300 | 1000–6000 |
| 3 | $\theta$ | 0.1–0.35 | 4–7 | 1000-2100 | 1000-1200 | 600–1300 | 1000–6000 |
| 4 | $\theta_{wind}$ | 0.1–0.35 | 4–7 | 1000-2200 | 1000–1150 | 600–1300 | 1000–6000 |
| 5 | Wind Mag. | 0.1–0.35 | 3.5–6 | 1000–2100 | 975–1200 | 600–1300 | 1000–6000 |
| 6 | Wind Mag. | 0.1–0.35 | 3.5–7 | 1000–2200 | 975–1200 | 600–1300 | 1000–6000 |
| 7 | Wind Mag. | 0.1–0.35 | 3.5–7 | 1000–2100 | 975–1200 | 550–1300 | 1000–6000 |
| 8 | $H_{sig}$ | 0.15–0.6 | 6.5–8 | 500–1800 | 700–1100 | 200–1100 | 800–4000 |
| 9 | $H_{sig}$ | 0.25–0.8 | 7–8 | 250–1500 | 500–1100 | 150–900 | 250–2500 |
| 10 | $H_{sig}$ | 0.3–1.2 | 7.5–8 | 150–1200 | 400–1100 | 100–700 | 150–2000 |
| 11 | $T_p$ | 0.1–0.45 | 4–8.5 | 700–2000 | 900–1150 | 400–1200 | 1000–4500 |
| 12 | $T_p$ | 0.15–0.45 | 4.5–9.5 | 550–1800 | 800–1150 | 300–1100 | 900–4000 |
| 13 | $T_p$ | 0.05–0.3 | 3.5–6 | 1200–2300 | 1050–1200 | 700–1350 | 1900–6750 |
| 14 | $\theta_{wind}$ | 0.1–0.35 | 4.5–7 | 1100–2100 | 975–1200 | 500–1300 | 1200–6000 |
| 15 | $\theta_{wind}$ | 0.1–0.35 | 4–7.25 | 1000–2100 | 975–1200 | 550–1300 | 1200–6000 |
| 16 | $\theta$ | 0.1–0.35 | 4.5–7 | 1000-2100 | 975–1200 | 500–1250 | 1150–5250 |
| 17 | SE | 0.15–0.35 | 3–7 | 900–2100 | 950–1200 | 575–1200 | 1250–5000 |
| 18 | SE & $H_{sig}$ | 0.2–0.55 | 6.5–7.5 | 500–1500 | 750–1100 | 250–900 | 500–3000 |
| 19 | SE & $H_{sig}$ | 0.3–0.8 | 7.5–8 | 275–1100 | 550–1000 | 200–750 | 300–1500 |
| 20 | SE & $H_{sig}$ | 0.4–0.9 | 7.9–8.5 | 175–900 | 400–1000 | 100–500 | 175–1500 |
| 21 | SE & $T_p$ | 0.15–0.4 | 4.5–8 | 800–1800 | 900–1400 | 500–1100 | 1000-3500 |
| 22 | EX $H_{sig}$ | 1.2–2.3 | 11–13.5 | 50–200 | 100–450 | 25–100 | 35–225 |
| 23 | EX, SE, $H_{sig}$ | 0.6–1.6 | 8–10 | 100–300 | 200–600 | 50–200 | 100–400 |
| 24 | EX, $T_p$ | 0.4–1.3 | 11.5–14.5 | 100–600 | 300–850 | 75–350 | 100–900 |

waves had noticeable effects on the factor of safety values. All trials with $T_p$ greater than the MCC show reduced $F_{safety}$ ranges for all coral species, while trial 13 ( with a period of 7 s) saw $F_{safety}$ values above those of the MCC.

Increases in significant wave height at the boundaries had the greatest influence on increasing $u_{bot}$ ranges and decreasing $F_{safety}$ ranges (Table 5). Trials 8, 9 and 10 utilized boundary waves of 2.5, 3.5 and 4.5 m (respectively) with otherwise standard conditions. Bottom wave orbital velocity ranges increased from 0–0.4 (MCC), to 0.15–6 (Trial 8), to 0.25–0.8 (Trial 9), and finally to 0.3–1.2

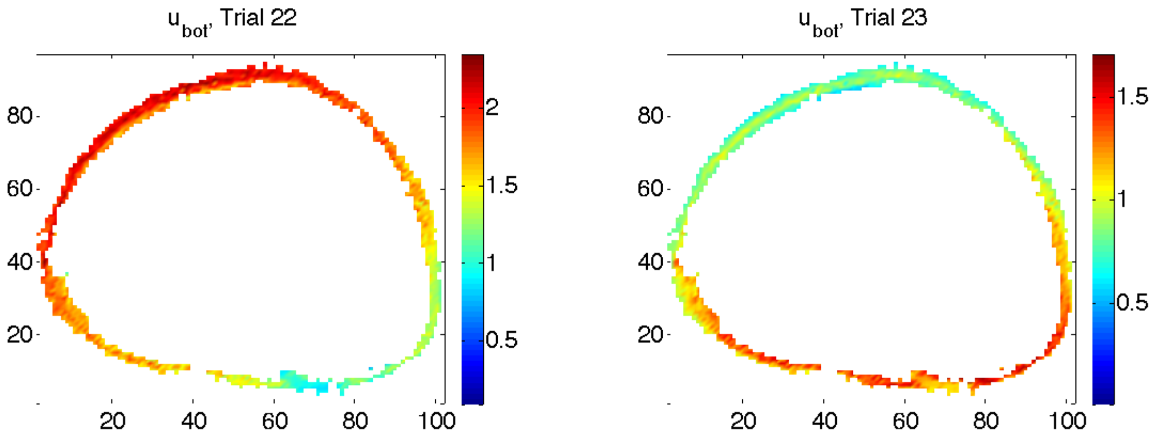

(a) SWAN modeled $u_{bot}$, Trial 22, depths: 10–20 m. (b) SWAN modeled $u_{bot}$, Trial 23, depths: 10–20 m.

Figure 9: Extreme significant wave height events, Trials 22 and 23. Trial 22 features swell with $H_{sig} = 9.2$ traveling in a direction of 296°, whereas Trial 23 has swell with $H_{sig} = 7.5$ m/s traveling at 86°.

m/s (Trial 10). Trials 8, 9 and 10 also show elevated $T_{m01}$ ranges relative to Trial 1 and the $\theta_{wind}$ trials. Additionally, the increases in $T_{m01}$ come from a 0.5 s increase in the lower range value for every 1 m increase in boundary $H_{sig}$. The trials of increasing $H_{sig}$ saw the lowest ranges for $F_{safety}$ outside of the extreme events analysis. In the order of Trial 8, Trial 9, and Trial 10, the coral species $F_{safety}$ ranges are: 500–1800, 250–1500 and 150–1200 for *P. meandrina*, 700–1100, 500–1100 and 400–1100 *P. lobata*, 200–1100, 150–900, and 100–700 for *M. capitata* and 1000-4500, 900–4000, 1900,6750 for *P. compressa*

Thus far, all the incoming waves discussed have come from the NW, at a direction of 295–315°and have impacted the north and west of the atoll, generating spatial distributions relatively similar to Fig 7. Trials 17–21 feature waves traveling at 105°, (headed north-northwest) and hitting the south and east edges of the Atoll (Fig 9). Significant wave heights from Table 3 were run for this new wave direction (Trials 17–20) because $H_{sig}$ had the greatest influence over $u_{bot}$. As with the ≈300° waves, increasing $H_{sig}$ at the boundaries caused increases in $u_{bot}$ and $T_p$, and the corresponding decreases

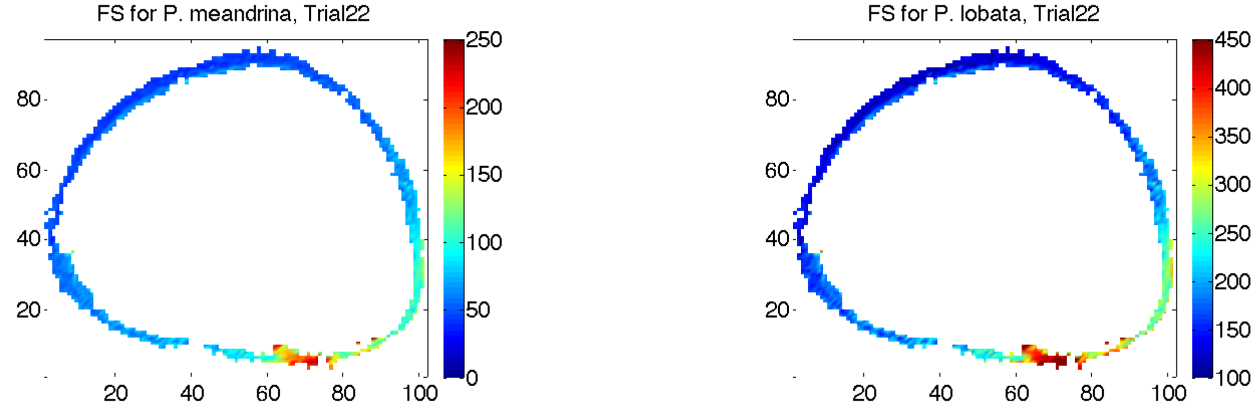

(a) Factor of Safety: *P. meandrina*, Trial 22 (b) Factor of Safety: *P. lobata*, Trial 22

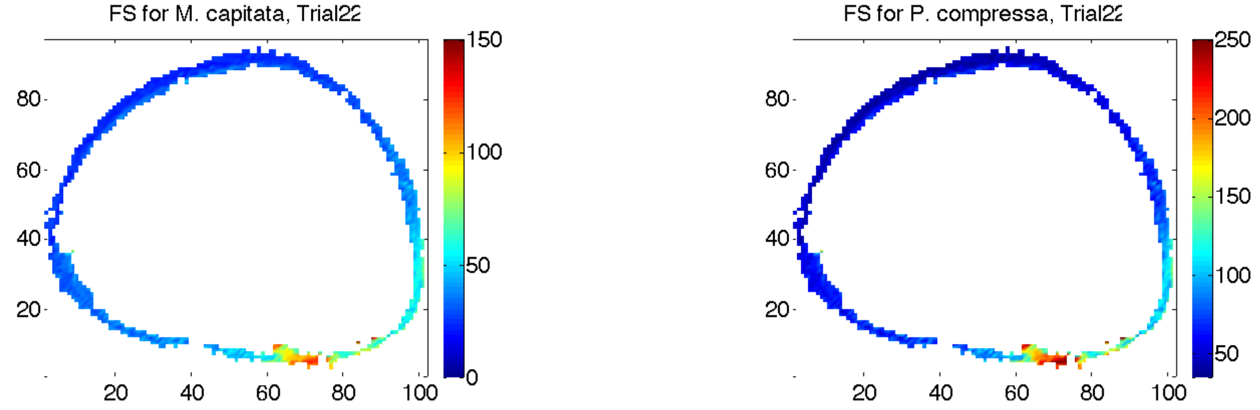

(c) Factor of Safety: *M. capitata*, Trial 22 (d) Factor of Safety: *P. compressa*, Trial 22

Figure 10: Extreme Event: Trial 22 $H_{sig} = 19.2$ m, $T_p = 16$ s, $\theta = 296°$, wind magnitude = 13.5 m/s and $\theta_{wind} = 139°$

in $F_{safety}$ values (Table 5). A slight difference between the 105°waves and the northwesterly swell is that while 105°waves did not create as high of $u_{bot}$ ranges (see Trial 10 vs Trial 20), Trials 19 & 20 showed greater mean period ranges than their ≈300°counterparts. Coral factor of safety ranges were similar to those in Trials 1 and 8–10, with better fitting on the lower end of the ranges, and, because coral failure is one of the chief concerns of this project, the lower end of the range is the primary concern when discussing $F_{safety}$ values. Finally, Trial 21, which had a significant wave height of 1.5 m but a period of 11 s, was run for 105°. The alterations to $u_{bot}$, $T_p$ and species-specific $F_{safety}$ relative to the MCC condition for 105°(Trial 17) were similar to differences between Trials 11 and 1.

### 4.3 Extreme Events

The two significant wave height extreme events (Trials 22 and 23) both demonstrate the influence of high energy swell on the entire Atoll. The largest event, Trial 22, featured $u_{bot}$ ranges of 1.2–2.3 m/s, and even generated a significant $u_{bot}$ velocity in the sheltered bay south of Green Island (see Figs 7a & 9a). The mean period ranged from 11–13.5 s, lower than the original peak period of 16 s, and second only to the high-period extreme event (Trial 24) in terms of magnitude. Trial 22 generated the lowest $F_{safety}$ values of all the trials, with *P. meandrina* ranging from 50 to 200, *P. lobata* from 100 to 450, *M. capitata* from 25 to 100, and *P. compress* ranging from 35 to 225 units. The 7.5 m swell in Trial 23 was also able to generate $u_{bot}$ around the entire atoll, with bottom wave orbital velocities of nearly 1 m/s on the north and west edges (Fig 9b). Coral safety factors for Trial 23 were the second lowest in the data set (Table 5), with the lower ends of the ranges being around double those of Trial 22. The final extreme event was the highest daily period from the WWIII data, a period of 17.6 s with 3.4 m swell traveling at 319°. This event generated $u_{bot}$ values of 0.4–1.3 m/s, and had the third lowest collection of $F_{safety}$ values: *P. meandrina* 100–600, *P. lobata* 300–850, *M. capitata* 75–350, and *P. compressa* 100–900 units.

# 5 Discussion

## 5.1 What's wrong with $F_{Safety}$?

Comparing the $F_{safety}$ values of this study (Table 5) to those of Storlazzi et al. [2005], it is immediately apparent that something here is amiss. $F_{safety}$ values presented by Storlazzi et al. [2005] were largely in the range of 0–100, whereas this study had $F_{safety}$ values that rarely fell below 500. Additionally, *Porites compressa* is clearly shown to be the weakest of the coral species in Storlazzi et al. [2005]. In this study however, *P. compressa* often has the highest $F_{safety}$ range (Table 5). This result, that *P. compress* has the highest $F_{safety}$ range, seems rather odd, because otherwise the ranking of species' ranges is the same as Storlazzi et al. [2005]. The previous study ranked the species (in order of most to least resilient): *P. lobata*, *P. meandrina*, *M. capitata* and finally *P. compressa*; in this study, the ranking goes: *P. compressa* and then *P. lobata* to *M. capitata* as previously ranked.

For each trial, all species' $F_{safety}$ calculations utilized the same $a_{fluid}$ and other constants ($C_{lift}$, $\rho_{cor}$, etc.) and therefore this result is more likely to be a consequence of the coral measurements. *Porites compressa* is the smallest of the corals evaluated (Table 6), and when ranked according to size (with *P. meandrina* larger than *M. capitata* due to $r_{cor}$ and $r_{base}$) the lineup matches the $F_{safety}$ rankings of Storlazzi et al. [2005]. Is the condition of corral breaking then largely reliant on the size of the coral? This question is difficult to answer. Certainly the rankings do not correlate exactly to mechanical strength ($\sigma_{mean}$), for which *P. meandrina* has the highest value (7.0 MPa, Table 6). Nor do the rankings of the ratio of $r_{cor}/r_{base}$, for which *P. lobata* and *P. compressa* are closer to each other than to the other two species (Table **??**). From Massel [2013], we know that the coral is likely to break at the base because the horizontal forces (Eq 24 & **??**) create an overturning

Table 6: Comparing the rankings of different coral measurement (Table 6) combinations

| Species | Size | $\frac{r_{cor}}{r_{base}}$ | $\frac{r_{cor}h_{cor}}{\pi r_{base}^2}$ |
|---|---|---|---|
| *Montipora capitata* | 3 | 1.667 | 1.764 |
| *Porites compressa* | 4 | 1.000 | 2.387 |
| *Porites lobata* | 1 | 1.111 | 0.786 |
| *Pocillapora meandrina* | 2 | 1.857 | 1.689 |

moment about the neutral axis of the coral, which is counteracted by the strength of the area of attachment: $A_{cb} = \pi r_{chase}^2$. Thus, the horizontal forces $F_{ci}$ and $F_{cd}$ act on the surface area (SA) of the coral above the base, and therefore a larger ratio of SA to $A_{cb}$ would result in a greater chance of failure. Interestingly, the SA:$A_c b$ ratio (Col. 4, Table 6) does properly match the Storlazzi et al. [2005] rankings, especially when one considers that *P. meandrina* has twice the mechanical strength of *M. capitata*, and would therefore be ranked second in terms of resilience.

The ratio, unfortunately, does not explain why this study has *P. compressa* as often having such a large $F_{safety}$ value. Indeed, all the values in this study are 2+ orders of magnitude larger than those of Storlazzi et al. [2005]; but with the exception of *P. compressa*, the trends are similar: declining $F_{safety}$ with increasing $u_{bot}$, and the ranking order of the other three species. Therefore, while the hydrodynamic model (the equations that generate $F_{safety}$) is not wholly broken, it is not properly generating values that match those of Storlazzi et al. [2005]. To understand why this is happening, it is important to examine all the differences between the two studies.

One of the early difficulties in incorporating the hydrodynamic model was the implementation of Eq 30. Equation 30 was used by Storlazzi et al. [2005] with a minus sign before the second term on the RHS (i.e. the tensional force [Massel 2013]), whereas this study used Eq 30 with a plus sign (i.e. the compressional force). The reason for the substitution was that the $\frac{1}{4}\pi r_{cbase}^4$ term on the RHS was being computed with very small values (Table 6) and this caused the second term on the RHS to be very large and $\sigma_{applied}$ to often become quite negative. Additionally, when the vertical forces (first term, RHS, Eq 30) were large enough to keep $\sigma_{applied}$ positive, the resulting value was quite small and resulted in $F_{safety}$ values on the order of $10^7$. Additional combinations of the tensional and compressional methods were applied to form the $\sigma_{applied}$ used in Eq 31, including the absolute value of the tensional force, the summation of the tensional and compressional forces, and the absolute value of the previous summation, but all of these methods produced $F_{safety}$ values even less like those of Storlazzi et al. [2005] Therefore, the compressional variation of $\sigma_{applied}$ was chosen, and it was thought that this choice was supported by Massel [2013] who stated that either strain could cause a coral to fail.

Next, as was briefly covered in the Methods, the acceleration of the fluid around the coral ($a_{fluid}$) was used by both Massel [2013] and Storlazzi et al. [2005] without an explicit definition of the function, the latter stating that $a_{fluid}$ was a function of $u_{bot}$ and $T_p$. This lead to the implementation of $a_{fluid} = u_{bot}/T_p$, for reasons explained previously. Because the exact formulation of $a_{fluid}$ was not known, it could have been miscalculated herein, creating a source of deviations from the published values of Storlazzi et al. [2005]. A related difference between the two studies was the use of the mean period rather than the peak period in calculating $a_{fluid}$, which is the only place in the Storlazzi et al. [2005] hydrodynamic model that the period is featured. Because the formulation of $a_{fluid}$ is not known, the difference between the two period metrics is difficult to assess. Regarding the use of $T_p$ or $T_{m01}$, it can be said that a larger period value (i.e. $T_p$) in this study would have decreased $a_{fluid}$, and therefore $\sigma_{applied}$, which would have resulted in increased $F_{safety}$ values and further deviation.

As of this writing, the cause of the large differences between the published $F_{safety}$ values and those of this study remains unknown. Certainly, a factor of $\frac{1}{100}$, applied to all the $F_{safety}$ results of this study could bring the values much closer to those of Storlazzi et al. [2005]. Doing so, however, would essentially increase the force applied to the coral or decrease the strength of the coral—and neither of these actions has any physical basis. Therefore, left without recourse for the uncharacteristically large $F_{safety}$ values, or the fact that what was the weakest coral in Storlazzi et al. [2005] is the most resilient coral in this study, the choice is to either abandon the generated data or press onward with the comparison. Due largely to time and resource limitations, the decision was to press onward, with the hope that the reader will bear in mind the myriad of problems that have plagued this dataset.

## 5.2 Comparison with Coral Distributions

From the outset, it is not wholly surprising that $F_{safety}$ values are so far above failure ($F_{safety} \leq 1$) because this study focused on modeling the most common conditions, and coral species should be able to stand up to such forcing. The only boundary conditions changes that had noticeable effects on $F_{safety}$ were increasing the wave energy entering the model, either by increasing $H_{sig}$ (which had the greatest effect) or $T_p$. Waves traveling at 305° generated the greatest bottom wave orbital velocities in the northwest octant, and the least in the opposite (southeast) octant (Fig 7a), and waves traveling at 105° generated the highest $u_{bot}$ in the south octant (Fig 8a). Unfortunately, because other directions were not modeled (the extreme events were in directions similar to the common conditions) the distributions of $u_{bot}$ for other areas are not available.

From the data of Kenyon et al. [2008], fore-reef coral cover is highest on the North, Northwest, and West octants of the atoll (15.7%, 15.6% and 16.0% of coral cover, respectively), in the midrange on the east (10.4% and northeast 11.3%) octants, and lowest on the southwest, south and southeast octants (7.2%, 5.4% and 2.4%, respectively). Interestingly, the highest coral covers are in the areas that receive the most consistent wave energy. Such a finding may indicate that perhaps the increased wave energy brings more nutrients and possibly aid in keeping polyps in the area. However, such a link would mean that the south and southwest areas (which receive the second most wave energy (Fig 6)) would have the second highest coral cover, which is not the case.

The ranges of $F_{safety}$ indicate that *P. compressa* would have the greatest chance of survival, however under common conditions, all corals would be fine in almost any wave situation. The data of Kenyon et al. [2008] reports that both *M. capitata* and *P. compressa* are virtuality absent on fore-reef, which is heavily dominated by *P. lobata* and to a lesser extent *P. meandrina*. *P. lobata* and *P. meandrina* have similar $F_{safety}$ ranges, and they were ranked 1 and 2 in terms of resilience by Storlazzi et al. [2005], which makes much more sense than the results of this study.

# 6 Conclusion

This project was a very interesting first attempt at high resolution modeling of potential coral breakage at Kure Atoll. Unfortunately, because direct comparisons with Storlazzi et al. [2005] are impossible (due to the lack of complete explanation of all the variables used), the results create more questions than they do answers. What can certainly be said is that the spatial variability of the results indicates the importance of increasing model resolution when looking at coastal processes. These areas often see rapid changes in bathymetry, and therefore must utilize models (like SWAN) which are capable of tracking the many details involved in modeling these areas. The oddities of the $F_{safety}$ values calculated in this study indicate sensitivity analysis of the force balance model may be necessary, in order to assess if the $u_{bot}$ values are truly the most important influence for coral breakage.

# 7 References

Boland, RC, B Zgliczynski, J Asher, A Hall, K Hogrefe, and M Timmers (2006). "Dynamics of debris densities and removal at the northwestern Hawaiian islands coral reefs". In: *Atoll Research Bulletin* 543, pp. 461–470.

Booij, N, CR Ris, and LH Holthuijsen (1999). "A third-generation wave model for coastal regions: 1. Model description and validation". In: *Journal of Geophysical Research* 104.C4, pp. 7649–7666. DOI: `10.1029/98JC02622`.

Cavaleri, L and P Malanotte-Rizzoli (1981). "Wind Wave Prediction in Shallow Water: Theory and Applications". In: *Journal of Geophysical Research* 86.C11, pp. 10, 961–10, 973. DOI: `10.1029/JC086iC11p10961`.

Dana, TF (1971). "On the reef corals of the world's most northern atoll (Kure: Hawaiian Archipelago)". In: *Pacific Science* 25.1, pp. 80–87.

Denny, MW (1988). *Biology and mechanics of the wave-swept environment.* Princeton, New Jersey: Princeton University Press.

— (1993). "Extreme drag forces and the survival of wind- and water-swept organisms". In: *Journal of Experimental Biology* 194, pp. 97–115.

Eldeberky, Y (1996). "Nonlinear transformations of wave spectra in the nearshore zone". PhD thesis. Delft University of Technology, Faculty of Civil Engineering. 203 pp.

Gerhart, PW, RJ Gross, and JI Hochstein (1993). *Fundamentals of fluid mechanics.* Menlo Park, California: Addison-Wesley.

Gove, JM, GJ Williams, MA McManus, SF Heron, SA Sandin, OJ Vetter, and DG Foley (2011). "Quantifying Climatological Ranges and Anomalies for pacific Coral Reef Ecosystems". In: *PLOS one* 8.

Grigg, RW (1998). "Holocene coral reef accretion in Hawaii: a function of wave exposure and sea level history". In: *Coral Reefs* 17, pp. 263–272.

GS, Aeby, JC Kenyon, JE Maragos, and DC Potts (2003). "First record of mass coral bleaching in the Northwestern Hawaiian Islands". In: *Coral Reefs* 22.3, p. 256.

Hasselmann, K (1962). "On the nonlinear energy transfer in a gravity-wave spectrum. Part 1. General Theory". In: *Journal of Fluid Mechanics* 12, pp. 481–500.

Hasselmann, K et al. (1973). *Measurements of wind-wave growth and swell decay during the Joint North Sea Wave Project (JONSWAP).* Report. Deutches Hydrographisches Institut. 12 pp.

Hoerner, SF (1965). *Fluid-dynamic drag practical information on aerodynamic drag and hydrodynamic resistance.* Report. Bricktown, New York: Hoerner Dynamics Drag Co.

Holthuijsen, LH (2007). *Waves in Oceanic and Coastal Waters.* Cambridge University Press, p. 404. ISBN: 9790521860284.

Janssen, PAEM (1991). "Quasi-linear theory of wind-wave generation applied to wave forecasting". In: *Journal of Physical Oceanography* 21.11, pp. 1631–1642. DOI: `10.1175/1520-0485(1991)021<1631:QLTOWW>2.0.CO;2`.

JC, Kenyon and RE Brainard (2006). "Second recorded episode of mass coral bleaching in the Northwestern Hawaiian Islands". In: *Atoll Research Bulletin* 543, pp. 505–523.

Jokiel, PL and KS Rodgers (2007). "Ranking coral ecosystem "health and value" for the islands of the Hawaiian Archipelago". In: *Pacific Conservation Biology* 13, pp. 60–68.

Kenyon, JC, Dunlap MJ, and GS Aeby (2008). "Community structure of hermatypic corals at Kure Atoll in the Northwestern Hawaiian Islands: Stemming the shifting baseline". In: *Atoll Research Bulletin* 559.

Kochin, NJ, IA Kibiel, and NV Roze (1963). *Theoretical Hydromechanics.* Moscow: Gos. Izdat Fiz.-Mat. Lt. 583 pp.

Komar, PD (1998). *Beach processes and sedimentation.* New Jersey, US: Prentice Hall.

Komen, GJ, L Cavaleri, M Donelan, K Hasselmann, S Hasselmann, and Janssen PAEM (1994). *Dynamics and Modelling of Ocean Waves.* Cambridge: Cambridge University Press, 532 pp.

Lough, JM and DL Barnes (1992). "Comparison of skeletal density variations in *Porites* from the Central Barrier Reef". In: *Journal of Experimental Marine Ecology* 155, pp. 1–25.

Massel, SR (2013). *Ocean Surface Waves. Their Physics and Prediction.* 2nd ed. Advanced Series on Ocean Engineering (Book 36). World Scientific Publishing Company. 692 pp.

Mastenbroek, C, G Burgers, and PAEM Janseen (1993). "The Dynamic Coupling of a Wave Model and a Storm Surge Model through the Atmospheric Boundary Layer". In: *Journal of Physical Oceanography* 23, pp. 1856–1866. DOI: `10.1175/1520-0485(1993)023<1856:TDCOAW>2.0.CO;2`.

Miles, JW (1957). "On the generation of surface waves by turbulent shear flow". In: *Journal of Fluid Mechanics* 3, pp. 185–204. DOI: `10.1017/S0022112057000567`.

Milne-Thompson, LM (1960). *Theoretical Hydrodynamics.* London, UK: Mac Millan Press Ltd. 743 pp.

NOAA Pacific Islands Fisheries Science Center: Coral Reef Ecosystem Division & Pacific Islands Benthic Habitat Mapping Center (2007). *Gridded bathymetry and IKONOS estimated depths of Kure Atoll, Hawaii, USA.* URL: `http://www.soest.hawaii.edu/pibhmc`.

Pacific Islands Benthic Habitat Mapping Center (PIBHMC) (2011). *Northwest Hawaiian Islands: Kure Atoll.* URL: `http://www.soest.hawaii.edu/pibhmc/pibhmc_nwhi_kur_backscat.htm`.

Rodgers, K, Newston C, and Cox E (2002). "Effects of mechanical fracturing and experimental trampling on Hawaiian corals". In: *Environmental Management* 31.3, pp. 377–384.

Storlazzi, CD, EK Brown, Field ME, K Rodgers, and PL Jokiel (2005). "A model for wave control on coral breakage and species distribution in the Hawaiian Islands". In: *Coral Reefs* 24, pp. 43–55. DOI: `10.1007/s00338-004-0430-x`.

The SWAN Team (2013a). *SWAN Scientific and Technical Documentation.* Delf University of Technology, The Netherlands. URL: `http://www.swan.tudelft.nl`.

— (2013b). *SWAN User Manual.* Delf University of Technology, The Netherlands. URL: `http://www.swan.tudelft.nl`.

Tolman, HL (1992). "Effects of Numerics on the Physics in a Third-Generation Wind-Wave Model". In: *Journal of Physical Oceanography* 22.10, pp. 1095–1111. DOI: `10.1175/1520-0485(1992)022<1095:EONOTP>2.0.CO;2`.

— (2002). *User manual and system documentation of WAVEWATCH-III version 2.22.* Unpublished. NOAA / NWS / NCEP / MMAB, p. 133.

— (2009). *User manual and system documentation of WAVEWATCH III version 3.14.* Unpublished. NOAA / NWS / NCEP / MMAB, p. 194.

Zijlema, M, GPh van Vledder, and LH Holthuijsen (2012). "Bottom friction and wind drag for wave models". In: *Coastal Engineering* 65, pp. 19–26.